Viser Technology Pte. Ltd.
Research and Application of Materials Science
DOI: 10.33142/rams.v7i1.18642

Research Article Open Access

Comparison and Verification of the Potential Applicability of $BaTi_4O_9$ in the Field of Photocatalytic H_2 Evolution

Mengjie CUI[1], Imran MUHAMMADA[1], Tiezhen REN[1*], Xinwei YANG[2], Pengfei LIU[2], Xiaoming WU[2]

1. State Key Laboratory of Chemistry and Utilization of Carbon Based Energy Resources and Key Laboratory of Coal Clean Conversion & Chemical Engineering Process (Xinjiang Uyghur Autonomous Region), College of Chemical Engineering, Xinjiang University, Urumqi, Xinjiang 830046, China
2. Xinjiang Joinworld Company, Urumqi, Xinjiang, 830013, China

[*]***Corresponding Author:*** *Tiezhen REN, E-mail: rtz@xju.edu.cn*

Abstract

Photocatalytic hydrogen evolution is of great importance with the proceeding of dual carbon goals, for inorganic catalysts have been explored with high efficiency. The structure and properties of oxide composites might take advantage of each compound and display an increased activity. In our previous study, boron doped-$Cu_3Ni/BaTi_4O_9$ possessed a porous structure and its photocurrent response was apparent. To further verify its excellent catalytic activity, Al_2O_3, and SiO_2 were selected to replace with $BaTi_4O_9$ to prepare different composites. The physical and chemical features of each sample were characterized with SEM, XRD, XPS, etc. to reveal their structural variations. Correspondingly, the H_2 evolution rate was investigated with gas chromatography under the sunlight irritation. A distinct hydrogen yield was recorded with prepared samples. Further, the projected density of states analysis was taken through density functional theory calculations to appreciate the conduction band of the composite. The offered electrons during the photocatalytic process and the potential applicability of composites in the field of photocatalysis was verified.

Keywords: *Photocatalytic H_2 evolution; B doped $Cu_3Ni/BaTi_4O_9$; Porous structure; DFT calculation*

1 Introduction

Oxygenated materials are one of the most important catalysts, playing an irreplaceable role in various fields of photocatalysis, such as photocatalytic H_2 evolution, organic matter degradation, and CO_2 reduction. Various inorganic oxygen materials have attracted widespread attention and applied by researchers [1]. Such as $BaTi_4O_9$ (BTO) has a pentagonal prism tunnel structure and is a semiconductor with a bandgap of 3.57 eV for the potential value in the photocatalytic processes [2,3].

The cost effective Al_2O_3 has excellent chemical stability and high thermostability [4] making it widely used in photocatalysis [5,6]. A notable example of its utilization in the preparation of Pt and Al_2O_3 layers was simultaneously loaded onto TiO_2 nanoparticles to obtain an $Al_2O_3/TiO_2/Pt$ composite material [7]. Due to the presence of plentiful defect sites in Al_2O_3/TiO_2, Al_2O_3 also serves as an excellent electron acceptor for TiO_2. The transfer of photo-generated electrons from TiO_2 to the defect level of amorphous Al_2O_3 greatly facilitates the separation of charge carriers [8]. This machanism leads to the initial H_2 evolution rate increased from 0.4 μM min^{-1} on TiO_2/Pt to 0.9 μM min^{-1} on $Al_2O_3/TiO_2/Pt$. Therefore, introducing Al_2O_3 onto TiO_2 could significantly enhance catalytic activity to generate H_2. Moreover, Yanet et al. [9] prepared Al_2O_3:Ce^{3+}/Ce^{4+} materials by using the sol-gel method for the photodegradation of phenol. It was found that the degradation rate of phenol by Al_2O_3 material with 1.0 wt.% Ce could reach 94 % after 3 h of photocatalytic reaction.

Besides that, SiO_2 has the advantages of high heat resistance and high specific surface area, making it suitable as a catalyst in high temperature reactions. Therefore, it has also been applied in the field of photocatalysis. Experimental indicate that the composite material of TiO_2 and SiO_2 has high Ti^{3+} defects and oxygen vacancy. Through close contact of SiO_2/TiO_2 composite material with CaP to form a Z-type photocatalyst, the H_2 evolution rate could respectively reach 80.1 μmol g^{-1} and 94.0 μmol g^{-1} in pure seawater and artificial seawater within 4 h [11]. In addition, Wang et al. [10] successfully prepared ternary heterostructure catalysts $ZnIn_2S_4@SiO_2@TiO_2$ ($ZIS@SiO_2@TiO_2$) by simple sol-gel and solvothermal methods. Homogeneous mixing of TiO_2 and SiO_2 could form $SiO_2@TiO_2$

Received on March 10, 2025; Accepted on April 28, 2025

nanoparticles. Then the nanoparticles were uniformly inserted into the two-dimensional layered ZIS to form a ternary heterostructure, which effectively promotes the separation and transport of electrons (e^-) and holes (h^+). The 150%-ZIS@SiO_2@TiO_2 nanocomposites exhibited an excellent H_2 evolution rate (618.3 μmol g^{-1} h^{-1}) under visible light irradiation, and the Apparent Quantum Efficiency (AQE) at 380 nm could reach 17.56 %.

Several studies have substantiated the activity of Al_2O_3 and SiO_2 in the field of photocatalysis. In previous studies, our group discussed the modification of BTO with CuNi alloy and non-metallic element boron (B) for the photocatalytic H_2 evolution. To further verify the advantages of Cu_3Ni alloy and B on the activity of BTO and the potential of BTO in the photocatalysis field, alumina (Al_2O_3) and silicon oxide (SiO_2), were chosen to replace BTO in photocatalytic processes. The physical structures and photo-current of the prepared sample were investigated through the characterizations of the XRD, SEM, UV-vis, etc. The performance of H_2 evolution was revealed using gas chromatography. Following the hydrogen yield, the contributions of atomic states were investigated with the projected density of states analysis.

2 Experimental

2.1 Materials

All the reagents used in the experiment were of analytical grade without any further purification. $BaCO_3$, TiO_2, KCl, $BaCl_2$, and $Bi_4Ti_3O_{12}$ were brought from Sinopharm Chemical Reagent Co., Ltd, while AlOOH was provided by Xinjiang ZhongHe Co., Ltd. The rice husk (RH) and 30T/D electron-assisted thermal decomposition treatment equipment were provided by Harbin Dingdi Technology and Environmental Protection Co., Ltd. The Cupric Acetate Monohydrate ($Cu(CH_3COO)_2·H_2O$, 99.0 %), Nickel Acetate ($Ni(CH_3COO)_2·4H_2O$, 99.0 %), and Sodium Borohydride ($NaBH_4$, 98 %) were purchased from Tianjin Yongsheng Chemical Co., Ltd. Additionally, the triethanolamine (TEOA, 97 %) and C_3H_8O was purchased from Aladdin Reagent (Shanghai) Co., Ltd.

2.2 Preparation of BTO photocatalyst

BTO was synthesized using the molten salt method. The $BaCO_3$ and TiO_2 were mixed with molten salts (KCl and $BaCl_2$) and were milled for 8 h. Then, the slurries were mixed with the $Bi_4Ti_3O_{12}$ particles and ball-milled for 1 h. After drying, the reactants were heated at 1080 ℃ for 3 h. Then the powders were stirred in deionized water multiple times to remove salts, further put in a 2 mol L^{-1} of dilute nitric acid for 20 min to ensure that the oxides of Bi had reacted completely. Finally, the products were washed in deionized water several times to obtain pure BTO [11].

2.3 Preparation of Al_2O_3 photocatalyst

First, 1 g of AlOOH and 10 ml of C_3H_8O were mixed, and the mixture was respectively placed in a 70 ℃ constant temperature water bath for 8 h at 1500 R·min^{-1} high speed. Subsequently, , the mixture was transferred into a 100 ml autoclave with the Teflon lining for the hydrothermal reaction at a constant temperature of 200 ℃ for 24 h. Afterward, the substance was filtered and washed using deionized water and anhydrous alcohol. Then, the obtained products were dried for 30 min. The obtained precursor was respectively sintered at 600 ℃ for 2 h and the heating rate was 5 ^oC·min^{-1}. Finally, the white Al_2O_3 powder was collected.

2.4 Preparation of SiO_2 photocatalyst

The RH undergoes a simple sorting from the feeding port. It passes through a drying layer and is dried by hot gas at the bottom of the reaction device for 1 h. Next, enter the thermal decomposition layer. Here a stream of electron containing air (electrons injected into air) is fed into the device through the air inlet on the device wall by using a blower in the device center, which is helpful to increase the temperature of the hot zone. On the other hand, the radiation energy released by the ceramics, which was collected from the previous treatment, further reflects the reactor section and promotes the reactor temperature. After continuous treatment for 6 h, the furnace was shut down and the SiO_2 sample was collected.

2.5 Preparation of B(3)-Cu_3Ni/X photocatalyst

In brief, B(3)-Cu_3Ni/$Ba2Ti_4O_9$ was obtained with the following protocol. $Cu(CH_3COO)_2·H_2O$, $Ni(CH_3COO)_2·4H_2O$, and BTO were mixed with the mass ratio of 3:1:1 to get Cu_3Ni/$Ba_2Ti_4O_9$. In the mean time, 20 mL of 3%$NaBH_4$ was added and then with stirring till uniformly mixed at room temperature. Then the mixture was hydrothermal treated in an autoclave at 120 ^oC for 6 h. After cooling to room temperature, the precipitates were collected and washed with deionized water in sequence several times. Subsequently,, the solid sample was calcined at 600 ^oC for 2 h using N_2 as the carrier gas with a heating rate of 5 ^oC min^{-1} to obtain B(3)-Cu_3Ni/BTO. Correspondingly, B(3)-Cu_3Ni/Al_2O_3 and B(3)-Cu_3Ni/SiO_2 were prepared in same conditions.

2.6 Characterizations

To observe the morphology of the prepared samples, a scanning electron microscope (SEM) (Hitachi Electronics SU8010, Japan) was used. The structural information of the samples was characterized by the X-ray diffraction (XRD) using Bruker D8 Advance diffractometer (Bruker, Germany) with Cu-Kα radiation at 30 kV and 30 mA. The main functional groups of the sample were analyzed using the VERTEX 70 FTIR Spectrometer (Bruker Company,

Germany) using the KBr pellet method. To explore its photo response the UV-vis diffuse absorption spectra (Metash UV-8000, China) were used.

2.7 Photoelectrochemical tests

The photocurrent electrode was prepared as follows. 2 mg of the sample powder and 6 mL of ethanol were mixed with ultrasonic dispersion for 30 min. Then 100 μL of the suspension was uniformly dropped on the surface of prepared indium tin oxide (ITO) (2 cm × 2 cm) conductive glass. After the membrane was formed on the ITO substrate, it was cleaned with distilled water and ethanol in sequence for 1 h. Finally, the electrode was dried in an oven at 60 ℃ and an effective area of 4 cm^2 covered with the sample was successfully obtained.

The photocurrent response of samples was measured by the electrochemical workstation (Zahner ZENNIUM IM6) in a standard three-electrode system at room temperature. In the system, Ag/AgCl was the reference electrode and Pt/C acted as a counter electrode. The sodium sulfate solution (0.2 mol L^{-1}) was used as an electrolyte. The white light-emitting diode with the intensity of 10 mW·cm^2 was used as the light source, and the switching state of the light source was switched every 20 s [12].

The electrochemical measurements, including the electrochemical impedance test (EIS) and Mott-Schottky (M-S) test, were recorded with the electrochemical workstation. The electrolyte was set in 1 M of KOH solution.

2.8 Photocatalytic tests

In the photocatalytic H_2 evolution experiment, the 300W Xenon lamp, reaction device, and gas chromatography (Agilent 8860) were connected to calculate the H_2 evolution of photocatalysts. The 40 mg of photocatalyst and 8 mL of TEOA as the sacrificial agent were dispersed into a reaction apparatus containing 80 mL of pure water [13]. Simultaneously, cooling water was connected to maintain the photocatalytic process at approximately room temperature. The argon gas (Ar) was used as the carrier gas, and injected into the reactor for over 20 min to remove the air before illuminating.

After completing the blowing process, the actual H_2 evolution was tested by sampling with a GC analyzer at the 5th min of the initial reaction stage. Subsequently, sampling testing was conducted every 15 min for a total of 300 min, which is 5 h. Once the test was completed, the solid catalyst was dried in an 80 ^oC oven for 6 h through the centrifuge and washing steps, then the sample underwent 4 cycles of 5 h each to test its cyclic performance.

To calculate the AQE, we used a xenon lamp with various optical filters to obtain light with different wavelength ranges. It could be defined using an equation (1):

$$AQE = \frac{N_e}{N_p} \times 100\ \% = \frac{2n(H_2)}{N_p} = \frac{2n(H_2)(h \times c)}{I \times A \times \lambda} \times 100\ \% \quad (1)$$

In the above formula, $n(H_2)$ represents the number of H_2 molecules produced per second, I (W cm^{-2}) represents the energy of the light source per unit area, A (cm^2) represents the illuminated area, λ represents the wavelength of the incident light, h is the Planck constant, and c means the speed of light [14].

2.9 DFT calculations

The DFT was employed to investigate the electronic properties of B(3)-Cu_3Ni/BTO, B(3)-Cu_3Ni/Al_2O_3 and B(3)-Cu_3Ni/SiO_2 [15]. The system's properties are calculated by optimizing the corresponding model structure, including relaxing all atomic positions. The exchange correlation energy between electrons is described by the PBE (Perdew Burke Ernzerhof) functional under the generalized gradient approximation (GGA) [16,17], which is implemented in the CASTEP program of Device Studio [18]. A plane wave's cutoff energy is set to 300 eV, and the energy convergence standard is 2 × 10^{-5} eV per atom. The force on the relaxed atom is less than 0.02 eV $Å^{-1}$, and the Brillouin zone is sampled using a 4 × 4 × 1 grid. This method is used to calculate the density of states (DOS) of various catalysts. The highest energy level occupied by electrons is set to energy zero during the calculation process [19].

3 Results and Discussion

The microstructure of composites was observed through SEM. Figure 1a shows the BTO exhibits a dispersed and irregular nanosheet layered structure. Meanwhile, B(3)-Cu_3Ni/BTO photocatalyst displays an uneven porous surface with 1～2 μm macropores and a large number of abundant mesopores appearing (Figure 1b). The Al_2O_3 in Figure 1c exhibits agglomerated spherical nanoparticles with a particle size of approximately 30 nm [20,21]. However, the B(3)-Cu_3Ni/Al_2O_3 composite catalyst (Figure 1d) underwent significant changes, with the formation of 10 μm super large pits on the surface and formed unconnected hollow structures, which is not conducive to the transmission of electrons. This phenomenon might be due to the layering treatment of BTO, which makes it easier to form pores on the surface, while the agglomeration phenomenon of Al_2O_3 makes the surface more stable and more difficult to make pores. In Figure 1e represents irregularly large particles, with the agglomeration of crystalline grains, and the B(3)-Cu_3Ni/SiO_2 presents a rough surface with some agglomerated particles on it (Figure 1f).

The influence of different substances on the crystallinity was analyzed by XRD. As shown in Figure 2a, the diffraction peaks are located at 43.9 °, 53.1 °, and 75.1 °, corresponding to the (111), (200), and (220) crystal planes of Cu_3Ni alloy (JCPDS: 65-9048), respectively. The presence of (111) crystal plane corresponding to 43.93 ° is located between 45.38 ° of metal Ni (111) and 43.7 ° of metal Cu (111), indicating

the formation of Cu_3Ni alloy [22]. The main characteristic peaks at 23.26 °, 28.34 °, 30.11 °, 33.96 °, and 47.91 ° belong to the (301), (111), (211), (302), and (020) crystal planes of pure BTO (JCPDS: 77-1565)[23]. The characteristic peak corresponding to the (211) crystal plane of BTO in B(3)-Cu_3Ni/BTO tends to weaken. This might be due to the substitution of Ti or O in BTO by B atoms, which introduces defects changes the lattice parameters, and leads to structural intensity decreases [24]. This result indicates that B has been successfully doped into the BTO structure. The XRD peaks of Al_2O_3 (JCPDS: 29-0063) include the main peak at 37.36 °, 46.42 °, and 66.83 ° correspond to the (113), (004), and (044) crystal planes [25,26]. The characteristic peak of B(3)-Cu_3Ni/Al_2O_3 is mainly CuNi alloy, which may be due to the contribution of Al_2O_3 nanostructure. It is observed that the crystal structure of SiO_2 has strong characteristic peaks, which are consistent with cristobalite (JCPDS: 77-1317) and tridymite (JCPDS: 86-0681) [27]. Due to similar preparation conditions of these two crystal phases, when the crystallization temperature is below 1400 ℃, a cristobalite-tridymite (CT) structure will be formed [28]. The characteristic peaks of SiO_2 and CuNi alloy are both obvious in B(3)-Cu_3Ni/SiO_2. From the XRD results, it was observed that there are characteristic peaks of CuNi alloy in all three composites, and the characteristic peaks of BTO, Al_2O_3, and SiO_2 are also retained according to their relative strength as shown in Figure 2a. Notably, the strong characteristic peaks undergo slight shifts, which also proves that B replaces Ti, Al, and Si respectively, and connects with O to enter the BTO, Al_2O_3, and SiO_2.

The functional groups and chemical types of the catalyst was determined through FTIR analysis as depicted in (Figure 2b). Characteristic peak at approximately 621 cm^{-1} corresponds to the Ti-O stretching vibration of octahedral groups in complex perovskite structures, and the peak at 827 cm^{-1} displays the O-Ti-O stretching vibration, these characteristic peaks confirmed the presence of BTO [29]. The peaks at approximately 1655 ～ 1630 and 3400 ～ 3480 cm^{-1} correspond to the adsorbed water in the catalyst and the -OH on the surface [30,31]. The strong broadening band at 1000～400 cm^{-1} and two distinct peak bands indicate Al-O vibration [32]. Peaks around 1406 cm^{-1} and 1640 cm^{-1} are the bending vibration peaks of Al-OH [33], and several inconspicuous peaks in the broad peaks at low wavelengths, located at 1064 cm^{-1} and 746 cm^{-1}, respectively, representing the torsional and stretching vibrations of the Al-O bond [34,35]. SiO_2 shows peaks at 475 ～ 440 cm^{-1} and 870 ～ 805 cm^{-1}, represented by Si-O symmetric bending vibration and symmetric stretching [36]. Due to intermolecular dehydration, Si-O bonds polymerize to form Si-O-Si chains, which further indicates the presence of SiO_2 in the sample. The strong and wide peak is located in the region of 1100-1000 cm^{-1}, which is the transverse symmetric stretching vibration absorption peak of the Si-O-Si bond [37]. As the temperature of thermal decomposition increases, the characteristic peak here becomes sharper and smoother, indicating an increase in the purity of SiO_2 in the sample. Additionally, the peak near 1655～1630 cm^{-1} is the H-O-H bending vibration peak of water, which is a typical characteristic peak of white carbon black [38].

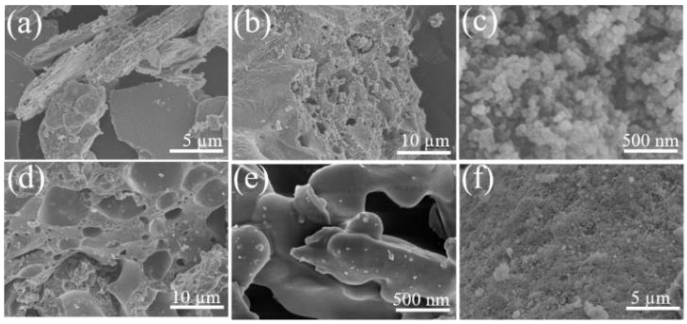

Figure 1 The SEM of (a) BTO, (b) B(3)-Cu_3Ni/BTO, (c) Al_2O_3, (d) B(3)-Cu_3Ni/Al_2O_3, (e) SiO_2 and (f) B(3)-Cu_3Ni/SiO_2

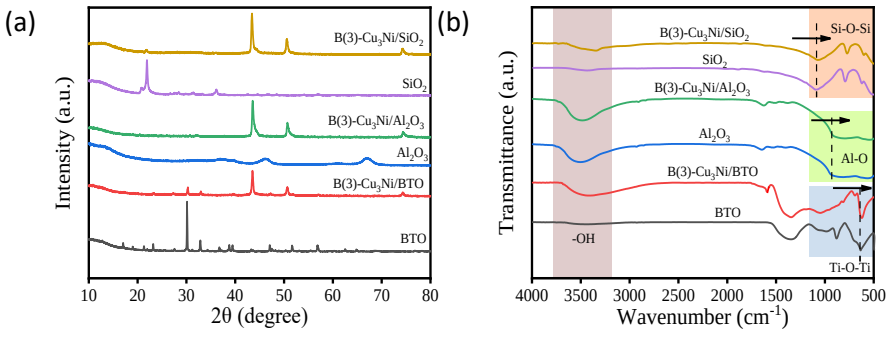

Figure 2 The (a) XRD spectra and (b) FTIR spectra of BTO, B(3)-Cu_3Ni/BTO, Al_2O_3, B(3)-Cu_3Ni/Al_2O_3, SiO_2 and B(3)-Cu_3Ni/SiO_2

With the doping of Cu_3Ni alloy, the intensity of the -OH peak at 3423 cm^{-1} significantly increases, indicating that Cu_3Ni could make the composite material more hydrophilic, which is conducive to the occurrence of photocatalytic water splitting reaction [39,40]. The comparison of the three composites shows that the Cu_3Ni alloy has a more significant effect on the surface functional groups of BTO. However, the vibration band of Cu_3Ni alloy in the complex is not detected because it is not active in FTIR and is not suitable for its detection [41]. Nevertheless, the characteristic peaks of the complex are consistent with their corresponding substances. Meanwhile, Due to the doping of B, the electronic structure of BTO, Al_2O_3, and SiO_2 have changed, resulting in the characteristic peaks of these substances all having a slight shift.

The photocatalytic activity is closely related to the light absorption performance of the photocatalyst. To explore the differences in optical properties between different oxides and corresponding composites, UV-vis tests were conducted (Figure 3a). The BTO has a lower absorption intensity in 410 ～ 1000 nm, with an absorption edge is around 410 nm. Al_2O_3 overall absorbance is the least, while SiO_2 exhibits superior absorbance in the visible light region, with an absorption edge is around 470 nm. It could be found that the light absorption ability of all three composites is significantly improved by modification with CuNi alloy and B, and the absorbance of B(3)-Cu_3Ni/BTO is the best.

To investigate the reason for photocatalytic activity increasing after B-doping, photoelectrochemical tests were conducted. In Figure 3b, all prepared photocatalysts exhibit repeatable photocurrent responses within each illumination cycle. During the switch light irradiation cycle, the photocurrent rapidly decreases in the dark. The photoelectric current response of composites is superior to that of pure oxides. B(3)-Cu_3Ni/BTO composite exhibits the highest photoelectric current response under visible light, followed by B(3)-Cu_3Ni/SiO_2, and finally B(3)-Cu_3Ni/Al_2O_3. This finding indicates that Cu_3Ni alloy and B greatly promote photocatalytic reactions making the composite have better separation efficiency for e^- and h^+ than pure oxides [42].

Then, an EIS test was conducted to clarify the charge transfer process at the interface between photocatalysts and electrolytes. The semicircle width in the high-frequency region reflects the charge transfer resistance (R_{ct}) [40]. In Figure 3c, the BTO has the smallest semi-circular diameter in the oxide, indicating that the charge at its interface is easily transferred to the surface to participate in the reaction[43]. The semicircles of all composites are smaller than their related oxides, meaning that the charge transfer resistance of the oxides after the composite of Cu_3Ni alloy and B is smaller, which is more conducive to the photocatalytic process. Among the composites, the semicircle diameter of the B(3)-Cu_3Ni/BTO is the smallest.

Meanwhile, the M-S curve generally describes the semiconductor properties of catalysts. A positive slope means an *n*-type semiconductor with e^- as carriers, while a negative slope means a *p*-type semiconductor with h^+ as carriers. From Figure 3d, both the oxide and its corresponding composites are *n*-type semiconductors with significant photocurrent response properties. As indicated the modification of Cu_3Ni and B do not alter the semiconductor properties of the catalyst. Comparing the test curves of all photocatalysts, the overall M-S curve of the composite material shows a significant increase, indicating an increase in free e^- in the catalyst after modification [44]. Especially, the slope of B(3)-Cu_3Ni/BTO is smaller than that of other catalysts, fitting to a faster rate of photogenerated charge transfer.

From the above tests, it could be found that the photoelectric characteristic pattern is BTO ＞ SiO_2 ＞ Al_2O_3. These correspond to the same sequence of the composites in the photocatalytic H_2 evolution reaction.

The effect of catalysts on the photocatalytic H_2 production process was investigated under a 300 W Xe lamp irradiation within 5 h, as shown in Figure 4a. BTO has the lower H_2 evolution, with only 9.11 μmol g^{-1} within 5 h. However, Al_2O_3 and SiO_2 do not produce H_2. During the first 30 min of the reaction, B(3)-Cu_3Ni/BTO has the highest H_2 evolution and could reach 1590.3 μmol g^{-1}. At the 300th min, the catalyst still participates in the reaction and produces H_2. However, the B(3)-Cu_3Ni/SiO_2 shows little H_2 evolution after 200 min, while B(3)-Cu_3Ni/Al_2O_3 showed little H_2 evolution after 150 min, resulting in the worst photocatalytic activity and stability.

Figure 4b shows the H_2 evolution rate of different oxides and corresponding composites. The maximum H_2 evolution rate of B(3)-Cu_3Ni/BTO is 318.06 μmol g^{-1} h^{-1}, is 101.18 times that of BTO (1.82 μmol g^{-1} h^{-1}), 6.69 times that of B(3)-Cu_3Ni/Al_2O_3 (47.57 μmol g^{-1} h^{-1}), and 3.61 times that of B(3)-Cu_3Ni/SiO_2 (88.12 μmol g^{-1} h^{-1}). The AQE of B(3)-Cu_3Ni/BTO, B(3)-Cu_3Ni/Al_2O_3, and B(3)-Cu_3Ni/SiO_2 samples were conducted. As shown in Figure 4c, the AQE matched well with the absorption spectrum. Moreover, the AQE of B(3)-Cu_3Ni/BTO is 8.91 % under the wavelength of 420 nm, which is significantly attributed to B(3)-Cu_3Ni/Al_2O_3 (1.33 %) and B(3)-Cu_3Ni/SiO_2 (2.47 %). The performance of the designed material was compared with previously reported work. It was observed that the prepared catalyst has a good hydrogen evolution rate, which can be attributed to its high surface porosity. Besides this, the prepared material water hydrogen evolution performance exhibits excellent cycling reactivity. After 4 cycles of experiments, Cu_3Ni/BTO the crystal structure of the catalyst has not changed, indicating that the catalyst has excellent cyclability [41], and the contaminant degradation reached up to 94% as compared to the previously reported literature [35]. Thus Cu_3Ni is suitable for BTO the composite ratio which will significantly improve the photocatalytic hydrogen production activity of the catalyst.

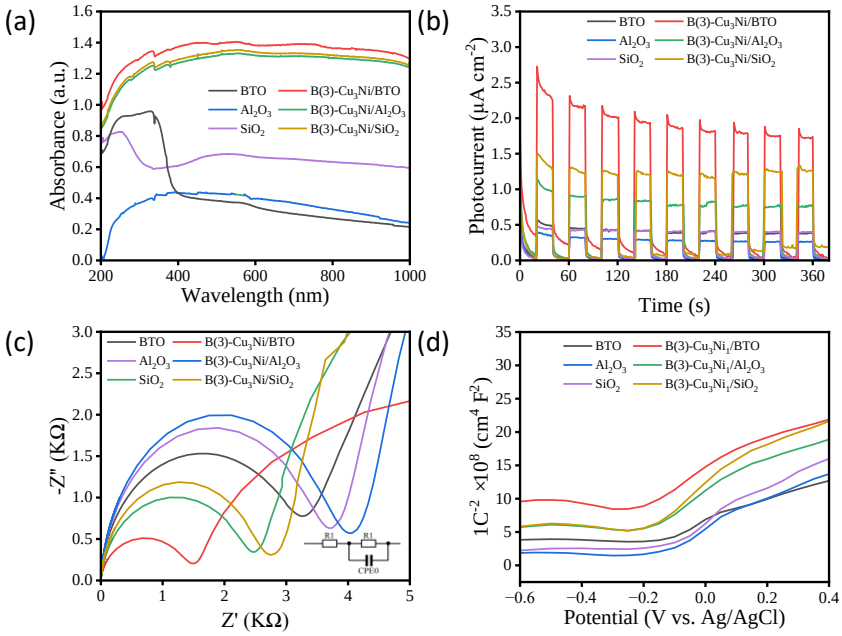

Figure 3 The (a) UV-vis absorbance spectra, (b) transient photocurrent density responses, (c) EIS spectroscopy, and (d) M-S spectroscopy of BTO, B(3)-Cu_3Ni/BTO, Al_2O_3, B(3)-Cu_3Ni/Al_2O_3, SiO_2 and B(3)-Cu_3Ni/SiO_2

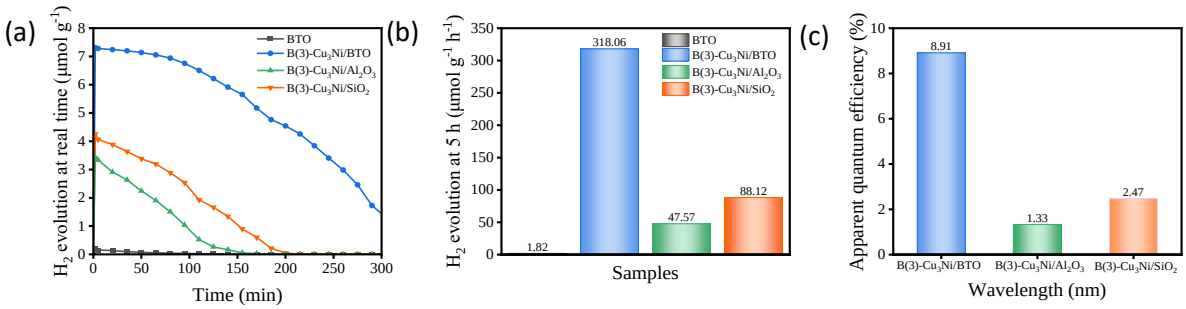

Figure 4 The real time photocatalytic H_2 evolution over time within 5 h under visible light irradiation (λ＞ 400 nm), and (b) H_2 evolution rate of BTO, B(3)-Cu_3Ni/BTO, B(3)-Cu_3Ni/Al_2O_3 and B(3)-Cu_3Ni/SiO_2; (c) The AQE value under 420 nm.

Based on the above performance testing results, it is elaborated that the H_2 evolution performance of the catalyst is consistent with the photoelectric characteristics, proving that BTO is more suitable for photocatalytic reaction processes. Different oxides not only affect the microstructure of the composite material but also alter its photocatalytic activity.

Combining the above analysis, the three different crystal structures were constructed by doping BTO, Al_2O_3, and SiO_2 with 3% B, separately. And the cell structures of composites are established by putting Cu_3Ni and oxides doped with B in the same space for DFT calculations. To compare the contributions of atomic states, Figure 5a shows the DOS and PDOS of the main atoms of B(3)-Cu_3Ni/BTO. The valence band (VB) of B(3)-Cu_3Ni/BTO is mainly composed of O 2p, while CB is composed of Ti 3d, Cu 2p, and Ni 2p, proving that after the composite of Cu_3Ni alloy and B(3)-BTO, CuNi alloy does indeed provide more free e^- for the CB of BTO to participate in the photocatalytic reaction. From Figure 5b, the VB of B(3)-Cu_3Ni/Al_2O_3 is mainly composed of Al 2p and O 2p, while CB is composed of Al 2p, with smaller contributions from other atoms. Compared with Figure 5a, the VB component in B(3)-Cu_3Ni/Al_2O_3 is composed of O 2p and Al 2p state cross-linking, indicating that the doping of 3% B has minimal effect on the electronic structure of Al_2O_3, and the minimum amount of e^- on the B(3)-Cu_3Ni/Al_2O_3 surface indicates that its catalytic activity is the lowest. In Figure 5c, the VB of B(3)-Cu_3Ni/SiO_2 is mainly composed of O 2p, while CB is composed of Si 2p and Cu 2p, with smaller contributions from other atoms. Moreover, the Si atom in B(3)-Cu_3Ni/SiO_2 provides a lower amount of e^- in CB, resulting in lower photocatalytic activity. The results obtained from DFT calculations are consistent with the experimental results, which also proves the accuracy of the experimental results.

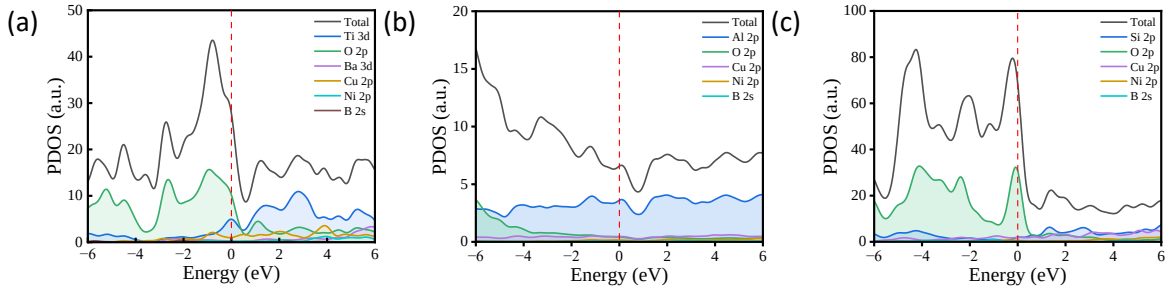

Figure 5 The DOS and PDOS plots for (a) B(3)-Cu_3Ni/BTO, (b) B(3)-Cu_3Ni/Al_2O_3, and (c) B(3)-Cu_3Ni/SiO_2. The black solid line represents the DOS rest of the color present PDOS in Figure 5a-c

4 Conclusions

The photocatalysis of hydrogen with B atoms doping in CuNi/BTO composite was discussed in the current research work. The conventional photocatalytic oxides (Al_2O_3 and SiO_2) were used to compare with BTO to explore the efficacy of BTO. Three different composites namely B(3)-Cu_3Ni/BTO, B(3)-Cu_3Ni/Al_2O_3, and B(3)-Cu_3Ni/SiO_2 were systematically investigated to demonstrate the advantages of BTO for photocatalysis. Notabley when, compared with Al_2O_3 nanoparticles and porous silicate, the BTO composite showed a high photo-current response and small resistance. Specifically, the B(3)-Cu_3Ni/BTO composite possessed a porous structure and exhibited superior optoelectronic properties and photocatalytic H_2 activity (318.06 μmol g^{-1} h^{-1}) than the corresponding nanoparticles. Moreover, the PDOS tests also proved that B(3)-Cu_3Ni/BTO could provide more e^- to participate in the redox reaction of photocatalytic reactions. The current finding demonstrates the practical significance, show casing the superior H_2 evolution rate of B(3)-Cu_3Ni/BTO (318.06 μmol g^{-1} h^{-1}). This result confirms the potential applicability of BTO in the field of photocatalysis and paves the way for the generation of high efficient material.

Acknowledgments: This work was supported by the Natural Science Foundation of Xinjiang Uygur Autonomous Region (2021D01A03), Key Research and Development Projects of Xinjiang Uygur Autonomous Region (2022B02038), Special Training Program for Scientific and Technological Talents of Ethnic Minorities in Xinjiang Uygur Autonomous Region (2020D03025), and Project of Tian chi talent leader in Xinjiang Uygur Autonomous Region (2022).

Reference

[1] W. M. ZHOU Shijie, REN Zhen, YANG Yusen, Preparation and application of metal oxides with various morphology for industrial catalysis [J]. CIESC Journal,2021(76):2972-3001.

[2] S. Ogura, K. Sato, and Y. Inoue, Effects of RuO_2 dispersion on photocatalytic activity for water decomposition of $BaTi_4O_9$ with a pentagonal prism tunnel and $K_2Ti_4O_9$ with a zigzag layer structure [J]. Physical Chemistry Chemical Physics, 2000(2):2449-2454.

[3] Y. Yamashita, K. Yoshida, M. Kakihana, et al. Polymerizable Complex Synthesis of $RuO_2/BaTi_4O_9$ Photocatalysts at Reduced Temperatures: Factors Affecting the Photocatalytic Activity for Decomposition of Water [J]. Chemistry of Materials,1999(11):61-66.

[4] M. Shekhar, J. Wang, W.-S. Lee, et al. Size and Support Effects for the Water-Gas Shift Catalysis over Gold Nanoparticles Supported on Model Al_2O_3 and TiO_2 [J]. Journal of the American Chemical Society, 2012(134):4700-4708.

[5] F. Li, Y. Zhao, Y. Liu, et al. Solution combustion synthesis and visible light-induced photocatalytic activity of mixed amorphous and crystalline $MgAl_2O_4$ nanopowders [J]. Chemical Engineering Journal, 2011(173):750–759.

[6] A. Zarubica, R. Ljupković, J. Papan, et al. Visible-light-responsive Al_2O_3 powder: Photocatalytic study. Optical Materials [J]. 2020(106):110013.

[7] W. Kim, T. Tachikawa, T. Majima, et al. Photocatalysis of Dye-Sensitized TiO_2 Nanoparticles with Thin Overcoat of Al_2O_3 : Enhanced Activity for H_2 Production and Dechlorination of CCl_4. The Journal of Physical Chemistry C [J]. 2009(113):10603–10609.

[8] F. Li, Y. Zhao, Y. Hao, et al. N-doped P25 TiO_2-amorphous Al_2O_3 composites: One-step solution combustion preparation and enhanced visible-light photocatalytic activity [J]. Journal of Hazardous Materials, 2012(239-240):118–127.

[9] Y. Piña-Pérez, F. Tzompantzi-Morales, R. Pérez-Hernández, et al. Photocatalytic activity of Al_2O_3 improved by the addition of Ce^{3+}/Ce^{4+} synthesized by the sol-gel method [J]. Photodegradation of phenolic compounds using UV light Fuel, 2017(198):11–21.

[10] L. Wang, H. Zhou, H. Zhang, et al. SiO_2 @TiO_2 Core@Shell Nanoparticles Deposited on 2D-Layered ZnIn2S4 to Form a Ternary Heterostructure for Simultaneous Photocatalytic Hydrogen Production and Organic Pollutant Degradation [J]. Inorganic Chemistry, 2020(59):2278–2287.

[11] L. Jin, Y. Huang, L. Zhang, et al. Formation mechanism of barium titanate single crystalline microplates based on topochemical transformation using bismuth-based

precursors [J]. Ceramics International, 2021(47):4543-4550.
[12] A. M. Hyde, S. L. Zultanski, J. H. Waldman, et al. General Principles and Strategies for Salting-Out Informed by the Hofmeister Series [J]. Organic Process Research & Development, 2017(21):1355-1370.
[13] S. Chen, J. Liao, Z. Zhou, et al. Boosting photocatalytic hydrogen evolution using a noble-metal-free co-catalyst: CuNi@C with oxygen-containing functional groups [J]. Applied Catalysis B: Environmental, 2021(291):120139.
[14] Z. Jiang, X. Xu, Y. Ma, et al. Filling metal-organic framework mesopores with TiO_2 for CO_2 photoreduction [J]. Nature, 2020(586):549–554.
[15] D. L. Chen Jingliang, Luan Lijun, Zhang Ru, et al. First-principles Calculation of Type-II C2N/ZnO Heterojunction as a Water Splitting Photocatalyst [J]. Materials Reports, 2023(37):21110258.
[16] W. Navarra, I. Ritacco, O. Sacco, et al. Density Functional Theory Study and Photocatalytic Activity of ZnO/N-Doped TiO_2 Heterojunctions [J]. The Journal of Physical Chemistry C, 2022(126):7000–7011.
[17] X. Tang, Q. Xue, X. Qi, et al. DFT and experimental study on visible-light driven photocatalysis of rare-earth-doped TiO_2 [J]. Vacuum, 2022(200):110972.
[18] M. Huang, Z. Zheng, Z. Dai, et al. DASP: Defect and Dopant ab-initio Simulation Package [J]. Journal of Semiconductors, 2022(43):042101.
[19] P. Ganguly, S. K. R., M. Muscetta, et al. New insights into the efficient charge transfer of ternary chalcogenides composites of TiO_2 [J]. Applied Catalysis B: Environmental, 2021(282):119612.
[20] Z. Gholizadeh, M. Aliannezhadi, M. Ghominejad, et al. High specific surface area γ-Al_2O_3 nanoparticles synthesized by facile and low-cost co-precipitation method [J]. Scientific Reports, 2023(13):6131.
[21] T.-P. Teng, Y.-H. Hung, T.-C. Teng, et al. Performance evaluation on an air-cooled heat exchanger for alumina nanofluid under laminar flow [J]. Nanoscale Research Letters, 2011(6):488.
[22] Z. Zhou, M. Wei, G. Yang, et al. Photoinduced electron-rich CuNi@C/TiO_2 catalyst for highly efficient hydrogen production from formaldehyde aqueous solution [J]. Journal of Alloys and Compounds, 2023(936):168360.
[23] X. Zhang, S. Tang, R. Li, et al. Synthesis and photocatalytic property of $BaTi_4O_9/RuO_2$ nanocomposites [J]. Materials Research Bulletin, 2013(48):609–612.
[24] A. N. Oliveros, J. A. I. Pimentel, M. D. G. de Luna, et al. Visible-light photocatalytic diclofenac removal by tunable vanadium pentoxide/boron-doped graphitic carbon nitride composite [J]. Chemical Engineering Journal, 2021(403):126213.
[25] G. Liu, J. Jiang, X. Wang, et al. Al_2O_3 nanoparticles modified the FeS_2 cathode to boost the interface wettability and electrochemical performance for thermal batteries [J]. Materials Letters, 2023(330):133290.
[26] L. Zhu, S. Pu, K. Liu, et al. Preparation and characterizations of porous γ-Al_2O_3 nanoparticles [J]. Materials Letters, 2012(83):73–75.
[27] I. M. Joni, L. Nulhakim, M. Vanitha, et al. Characteristics of crystalline silica (SiO_2) particles prepared by simple solution method using sodium silicate (Na_2SiO_3) precursor [J]. Journal of Physics: Conference Series, 2018(1080):012006.
[28] I. K. Moroz, G. N. Maslennikova, A. F. Mironova, et al. Formation of tridymite and cristobalite from quartz in porcelain [J]. Glass and Ceramics, 1980(37):147-150.
[29] A. Ali, S. Uddin, M. Lal, et al. Structural, optical and microwave dielectric properties of $Ba(Ti^{1-}xSnx)_4O_9$, $0 \le x \le 0.7$ ceramics [J]. Scientific Reports, 2021(11):17889.
[30] Z. Yan, K. Yin, M. Xu, et al. Photocatalysis for synergistic water remediation and H_2 production: A review [J]. Chemical Engineering Journal, 2023(472):145066.
[31] M. Ashour, I. Soliman, M. Mabrouk, et al. Silica Nanoparticles as a Potential Carrier for Doxycycline Hyclate [J]. Egyptian Journal of Biomedical Engineering and Biophysics, 2020(1034):40105.
[32] A. S. Jbara, Z. Othaman, A. A. Ati, et al. Characterization of γ- Al_2O_3 nanopowders synthesized by Co-precipitation method [J]. Materials Chemistry and Physics, 2017(188):24-29.
[33] S. Ponmudi, R. Sivakumar, C. Sanjeeviraja, et al. Influences of sputtering power and annealing temperature on the structural and optical properties of Al_2O_3:CuO thin films fabricated by radio frequency magnetron sputtering technique [J]. Journal of Materials Science: Materials in Electronics, 2019(30):18315-18327.
[34] A. Bazyari, Y. Mortazavi, A. A. Khodadadi, et al. Effects of alumina phases as nickel supports on deep reactive adsorption of (4,6-dimethyl) dibenzothiophene: Comparison between γ, δ, and θ-alumina [J]. Applied Catalysis B: Environmental, 2016(180):312-323.
[35] K. Atrak, A. Ramazani, and S. Taghavi Fardood, Green synthesis of amorphous and gamma aluminum oxide nanoparticles by tragacanth gel and comparison of their photocatalytic activity for the degradation of organic dyesalumina [J]. Journal of Materials Science: Materials in Electronics, 2018(29):8347–8353.
[36] L. Usgodaarachchi, C. Thambiliyagodage, R. Wijesekera, et al. Synthesis of mesoporous silica nanoparticles derived from rice husk and surface-controlled amine functionalization for efficient adsorption of methylene blue from aqueous solution [J]. Current Research in Green and Sustainable Chemistry, 2021(4):100116.
[37] M. M. Khayyat, G. K. Banini, D. G. Hasko, et al. Raman microscopy investigations of structural phase transformations in crystalline and amorphous silicon due to indentation with a Vickers diamond at room temperature and at 77 K [J]. Journal of Physics D: Applied Physics, 2003(36):1300–1307.
[38] M. Li, H. Shen, L. Zhuang, et al, SiO_2 Antireflection Coatings Fabricated by Electron-Beam Evaporation for Black Monocrystalline Silicon Solar Cells [J]. International Journal of Photoenergy, 2014(2014):1–5.
[39] J. Zhang, Y. Cao, F. Chen, et al. Tailoring hydrophilicity and electronic interactions and transfer: Enhancing hydrogen

production through size-tuned CuNi alloys [J]. Fuel, 2024(366):131364.
[40] R. Fang, Z. Yang, Z. Wang, et al. Transition metal tuned g-C_3N_4 induce highly efficient photocatalytic of ammonia borane to hydrogen evolution and mechanism investigation [J]. Fuel, 2023(334):126707.
[41] P. Zhang, G. Zeng, T. Song, et al. Synthesis of a plasmonic CuNi bimetal modified with carbon quantum dots as a non-semiconductor-driven photocatalyst for effective water splitting [J]. Journal of Catalysis, 2019(369):267–275.
[42] J. Li, Y. Huang, B. Luo, et al. Efficient photothermal-assisted photocatalytic hydrogen production over a plasmonic CuNi bimetal cocatalyst [J]. Journal of Colloid and Interface Science, 2022(626):975–984.
[43] T.-Z. Ren, M.-J. Cui, Y.-M. Zhao, et al. The Activated Carbon with Pyrolle-N from Cotton Stalk for the Electrochemical Performance [J]. Advanced Materials Science and Technology, 2022(4):79–92.
[44] T. Kou, M. Chen, F. Wu, et al. Carbon doping switching on the hydrogen adsorption activity of NiO for hydrogen evolution reaction [J]. Nature Communications, 2020(11):590.